Supplementary Information

Binary N,S-doped carbon nanospheres from bio-inspired artificial melanosomes: Route to efficient air electrode for seawater batteries

Ziyauddin Khan†, Sung O Park†, Juchan Yang, Seungyoung Park, Ravi Shanker, Hyun-Kon Song, Youngsik Kim, Sang Kyu Kwak*, and Hyunhyub Ko*

School of Energy and Chemical Engineering, Ulsan National Institute of Science and Technology (UNIST), Ulsan, 44919, Republic of Korea

*E-mail: skkwak@unist.ac.kr (S.K. Kwak), hyunhko@unist.ac.kr (H. Ko)

Experimental Section

Synthesis of melanosomes

In a typical synthesis of melanosomes, 30 mL of DI water, 13.13 mL of EtOH, and 0.25 mL of ammonium hydroxide were mixed and stirred in a round-bottomed flask under ambient conditions. After 30 min of continuous stirring, 0.167 g of a dopamine (Sigma Aldrich) solution in EtOH was injected into the above solution. After the addition of the dopamine solution, the solution color immediately changed to light brown and then changed to dark after some time. The reaction mixture was allowed to stir for 24 h under ambient conditions. Thereafter, melanosomes were collected via centrifugation, followed by washing with water and drying at 60 ℃ in a vacuum oven. This synthesis method was easily scalable.

Synthesis of N-doped carbon spheres (NCS)

NCS was synthesized via the pyrolysis of the prepared melanosomes at 800 ℃ for 4 h under nitrogen (Scheme 1). The ramp rate was maintained at 6 ℃/min.

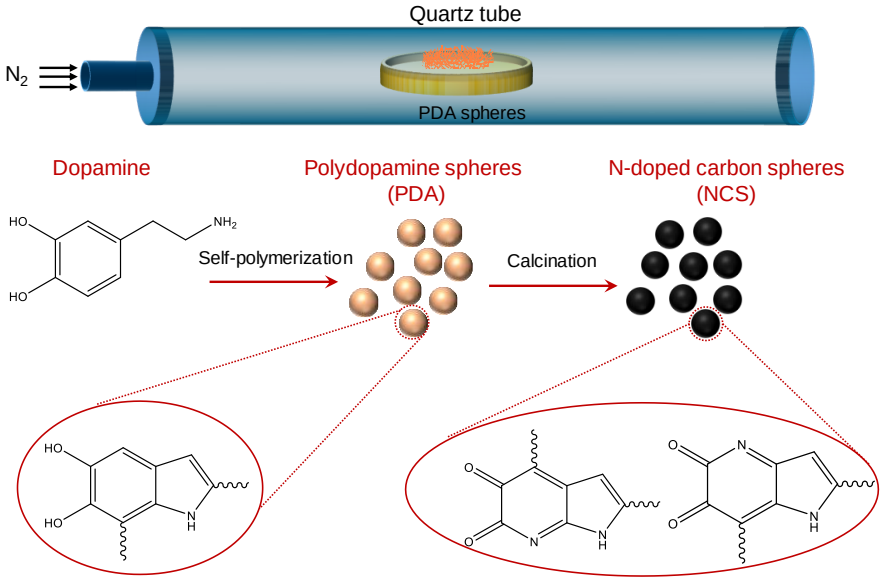

Scheme S1. Schematic of the synthesis of NCS prepared via the self-polymerization of dopamine followed by the pyrolysis of AMS under N_2.

Synthesis of N,S-doped carbon spheres (NSCS)

Binary elements, N and S, were simultaneously doped via the pyrolysis of melanosomes and S powder at 1:2 and 1:5 wt% under nitrogen atmosphere. First, melanosomes and S powder were added into separate alumina boats in different chambers of a chemical vapor deposition quartz tube. The S powder-containing chamber was heated at 600 ℃, whereas the melanosome-containing chamber was heated at 800 ℃ under flow of N_2 gas. Both chambers were maintained at their respective temperatures for 4 h. Notably, both precursors were not mixed, which ensured the absence of an external impurity of the S powder precursor in carbon and decreased the steps for product purification. The as-obtained powder was used for further characterization and study.

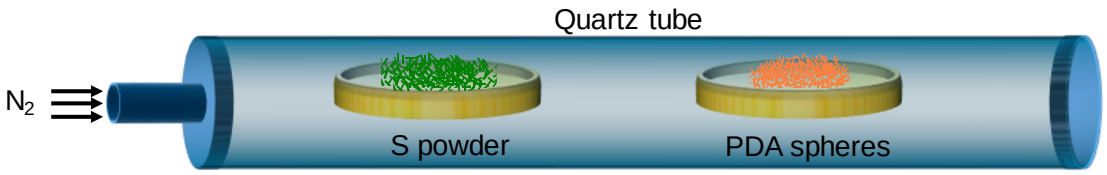

Scheme S2. Diagram of the quartz tube furnace and internal placement of the S and PDA powder for the synthesis of NSCS in a tube furnace.

Material characterization

The doping of N and S was investigated using X-ray photoelectron spectroscopy (XPS, K-Alpha, Thermo Fisher, Waltham, MA, USA). Confocal Raman microscopy (Alpha 300R, WITec, Ulm, Germany) with an excitation wavelength of 532 nm was employed to investigate the graphitic nature of carbon material. Surface morphologies of samples were recorded on a Hitachi S-4800 field-emission scanning electron microscope (FE-SEM) at an operating voltage of 10 kV. Transmission electron microscopy (TEM) samples were prepared by the

ultrasonication of the powder in ethanol and placement of the droplets of the as-prepared sample from the ethanolic dispersion on a Cu grid (200 mesh); the droplets were subsequently left to dry overnight. TEM and selected-area electron diffraction analyses were performed on a JEOL JEM 2100 high-resolution transmission electron microscope at an accelerating voltage of 200 kV. Energy-dispersive X-ray spectroscopy analysis was performed, and elemental maps were recorded on an INCA, Oxford Instruments system attached to the HR-TEM. BET surface areas were analyzed by nitrogen adsorption at liquid nitrogen temperatures on a Micromeritics ASAP 2020 nitrogen adsorption apparatus. All samples were degassed at 120 ℃ for 12 h before nitrogen adsorption–desorption measurements.

Electrocatalytic activity analysis

The electrocatalytic activity of catalysts was examined via rotating ring-disk electrode (RRDE) experiments using the catalyst as the working electrodes; Pt wire as the counter electrode; and Hg/HgO as the reference electrode in oxygen- and nitrogen-purged 0.1 M KOH solutions at scan rate of 10 mV s^{-1}. Catalyst inks (i.e., NCS, NSCS, and Super P carbon black) were prepared by mixing the catalysts in a ratio of 90:10 with Nafion (Sigma Aldrich) and drop-casting the inks onto the disk compartment of the ring-disk working electrode. Electrochemical characterization was performed using a Bipotentiostat (Iviumstat, Ivium Technologies, Eindhoven, Netherlands), and RRDE was rotated at speeds ranging from 400 to 3600 rpm using an RRDE controller (ALS RRDE-3A). The aqueous electrolyte was saturated with oxygen for ORR studies, whereas it was purged by nitrogen to measure the background currents.

Calculation of electron-transfer number

The electron-transfer number per oxygen molecule involved in the oxygen reduction reaction and fraction of peroxide ion (HO_2^-) formation (X) were estimated using RRDE method using equations (s1) and (s2), respsctively.[1-2]

$$n = \frac{4I_d}{I_d + I_r/N}, \quad \text{(s1)}$$

$$X = \frac{2\,I_r/N}{I_d + I_r/N}, \quad \text{(s2)}$$

where I_d is the disk current, I_r is the ring current, and N is the current collection efficiency of the Pt ring, which was determined to be 0.4.

Air electrode preparation

Air electrodes (i.e., NCS, NSCS, Pt/C, and Super P carbon black) were prepared by mixing electroactive material (90 wt%) and polyvinylidene fluoride (10 wt%) with 0.4 mL of N-methyl-2-pyrrolidone (NMP) to make a slurry, which was then coated on carbon paper (JNT20, JNTG, Korea) and dried overnight in a vacuum oven. The weight of the air electrode was 5 mg for each sample.

Cell fabrication for the static mode

The cell was fabricated as a pouch cell wherein the negative compartment was assembled in a glove box. Metallic Na was used as the negative and reference electrode, which was attached to nickel mesh, followed by its insertion in the pouch cell. Thereafter, an organic electrolyte (1 M $NaCF_3SO_3$ in tetraethylene glycol dimethyl ether, TEGDME) was injected as the negative electrolyte in the pouch cell. Finally, a NASICON-type ($Na_3Zr_2Si_2PO_{12}$) ceramic solid-

electrolyte membrane was used as separator, and the pouch cell was carefully sealed in the glove box. The solid-electrolyte membrane was placed in the pouch cell in such a way that one side was exposed to air, and the other side was in contact with the negative electrolyte. This solid-electrolyte membrane separated the non-aqueous negative electrolyte from the seawater positive electrolyte to avoid the direct contact of metallic Na with the aqueous electrolyte. The air electrode, in combination with the negative compartment, was dipped in the positive electrolyte such that one side was in direct contact with the solid-electrolyte membrane, whereas the other side was exposed for the diffusion of air and the electrolyte.

Cell fabrication for the flow mode

The design of the cell used in the flow mode was slightly different than that of a traditional 2032 coin-type cell. Here, the bottom part of the negative electrode comprising metallic Na and the negative electrolyte (1 M $NaCF_3SO_3$ in TEGDME) was sealed with the solid-electrolyte membrane (thickness of 0.8 mm and diameter of 16 mm). This cell was assembled in inert atmosphere. The air electrode with the negative electrode compartment was dipped in seawater flow cells (421 Energy Co., Ltd) with seawater (pH ~ 8) as the electrolyte.

Electrochemical performance analysis

The half-cell performances in the static and flow modes were analyzed using a battery cycler (WBCS3000, WonA Tech Co., South Korea). Power density was calculated by discharging the cell for 1 h at different current densities, and the terminated discharge voltage associated with each current density was examined. The observed discharge voltage (V) and current density (I) were multiplied for the calculation of the power density (P) of the cell.[3] Electrochemical impedance spectroscopy was performed using an impedance analyzer (Iviumstat, Ivium

Technologies, the Netherlands) at the open circuit voltage with an AC oscillation amplitude of 0.01 V over frequencies from 850 kHz to 0.1 Hz.

XPS spectra of C-PDA

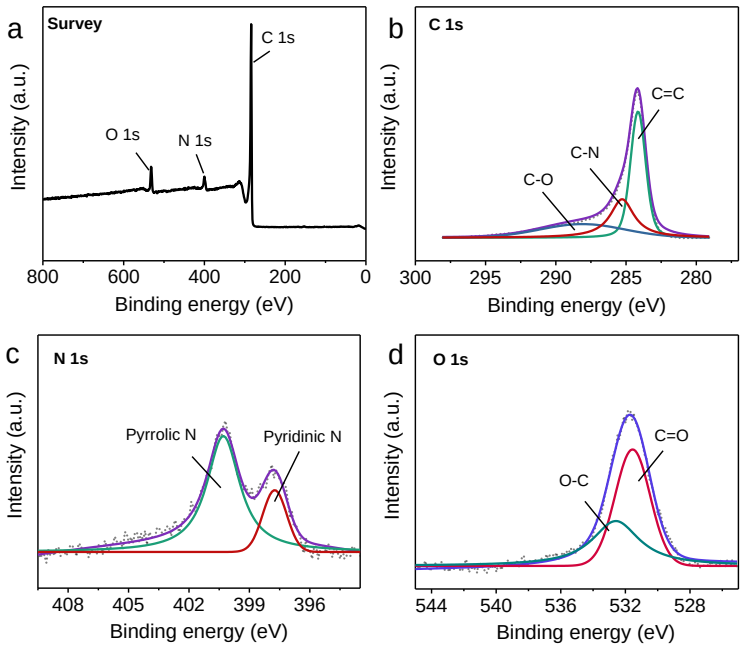

Figure S1. XPS (a) survey spectra and high-resolution spectra of (b) C 1s, (c) N 1s, and (d) O 1s of C-PDA derived from melanosome spheres.

Synthesis of NSCS using different weight percentage ratios of S powder

NSCS was also prepared with melanosomes and S powder in 1:2 and 1:5 wt% under similar experimental conditions. XPS survey spectra confirmed the presence of a higher S content in carbon at an AMS to S powder ratio of 1:5 (Fig. S2a and b). In addition, the morphology was examined via SEM, which revealed the formation of spherical carbon (Fig. S2c and d).

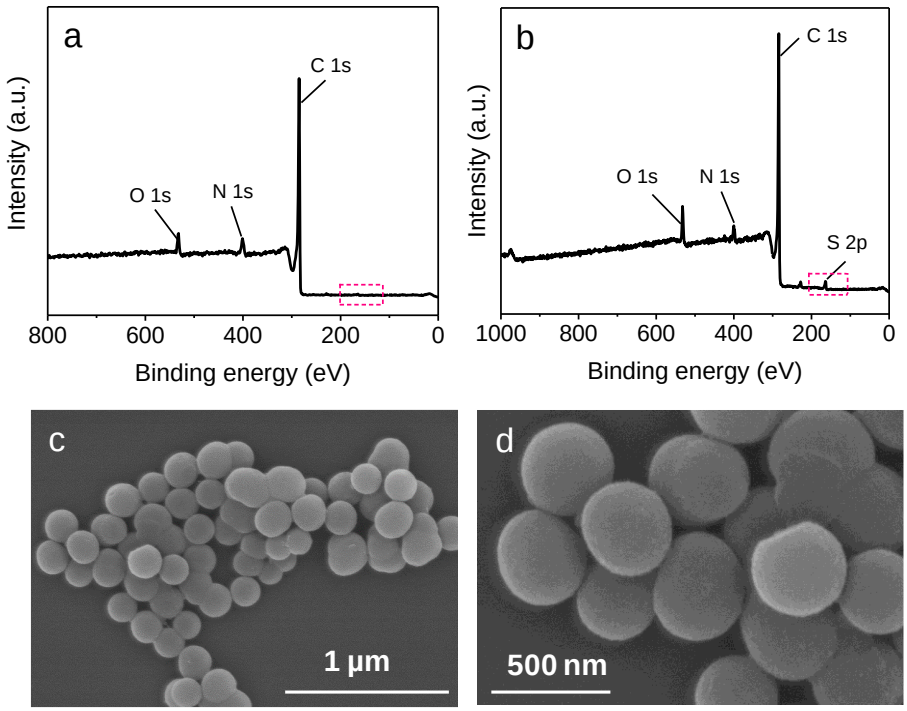

Figure S2. Survey spectra of NSCS when AMS:S (by wt%) is (a) 1:2 and (b) 1:5. Sulfur doping was more prominent using a high sulfur precursor. (c) and (d) are the SEM images of NSCS prepared by mixing melanosomes and S powder in 1:2 wt%.

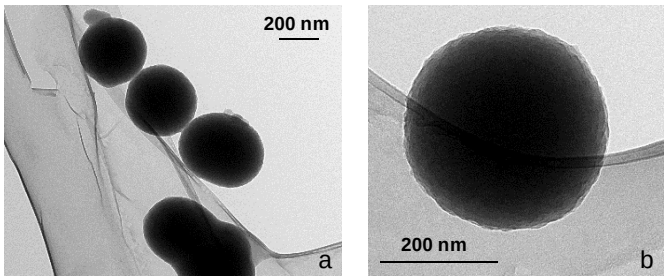

Figure S3. (a) Low- and (b) high-magnification TEM images of AMS.

SEM and TEM analysis of NCS

For the synthesis of NCS, AMS powder was pyrolyzed in a tube furnace at 800 ℃ for 4 h under N_2 atmosphere. After pyrolysis, the morphology of AMS spheres was maintained, as evident

from Fig. S4a–c. Energy-dispersive X-ray elemental maps revealed the uniform distribution of C, N, and O over the sphere (Fig. S4d–f).

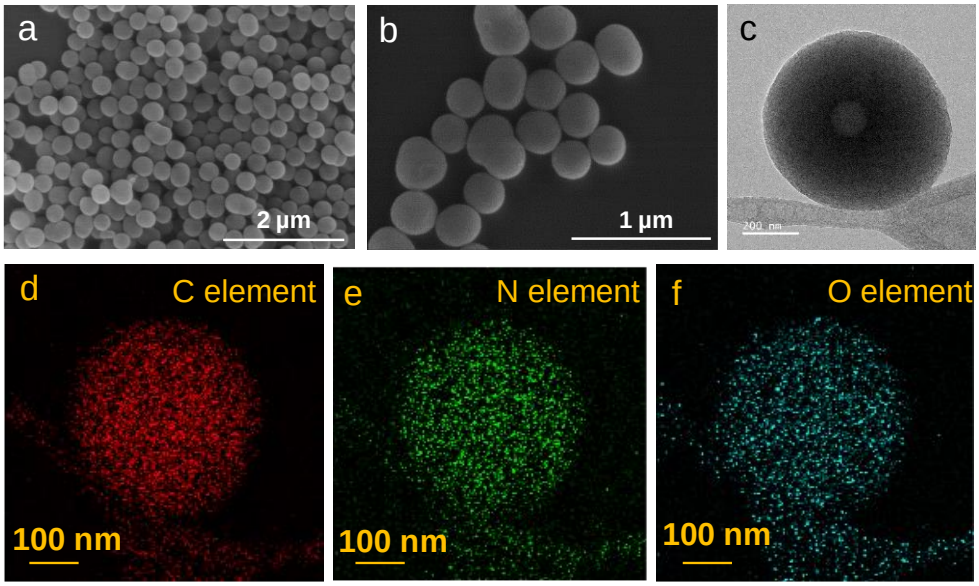

Figure S4. (a) Low-resolution and (b) high-resolution SEM images; (c) TEM image of NCS. Confirmation of (f) C; (g) N, and (h) O in NCS by elemental mapping images.

High resolution TEM image of NSCS

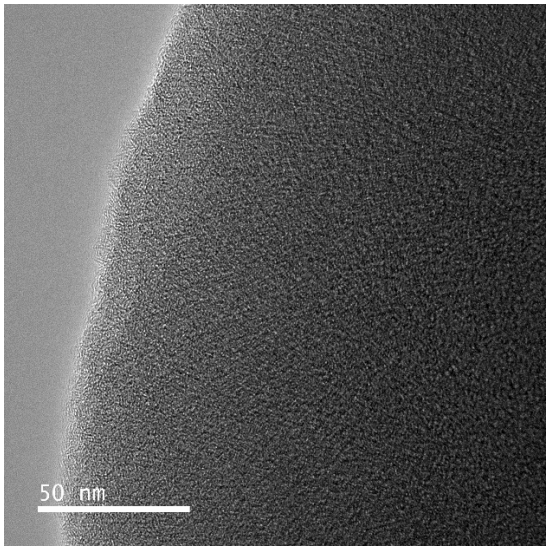

Figure S5. High resolution TEM image of NSCS.

BET surface area isotherms and pore volume plots of AMS and NSCS

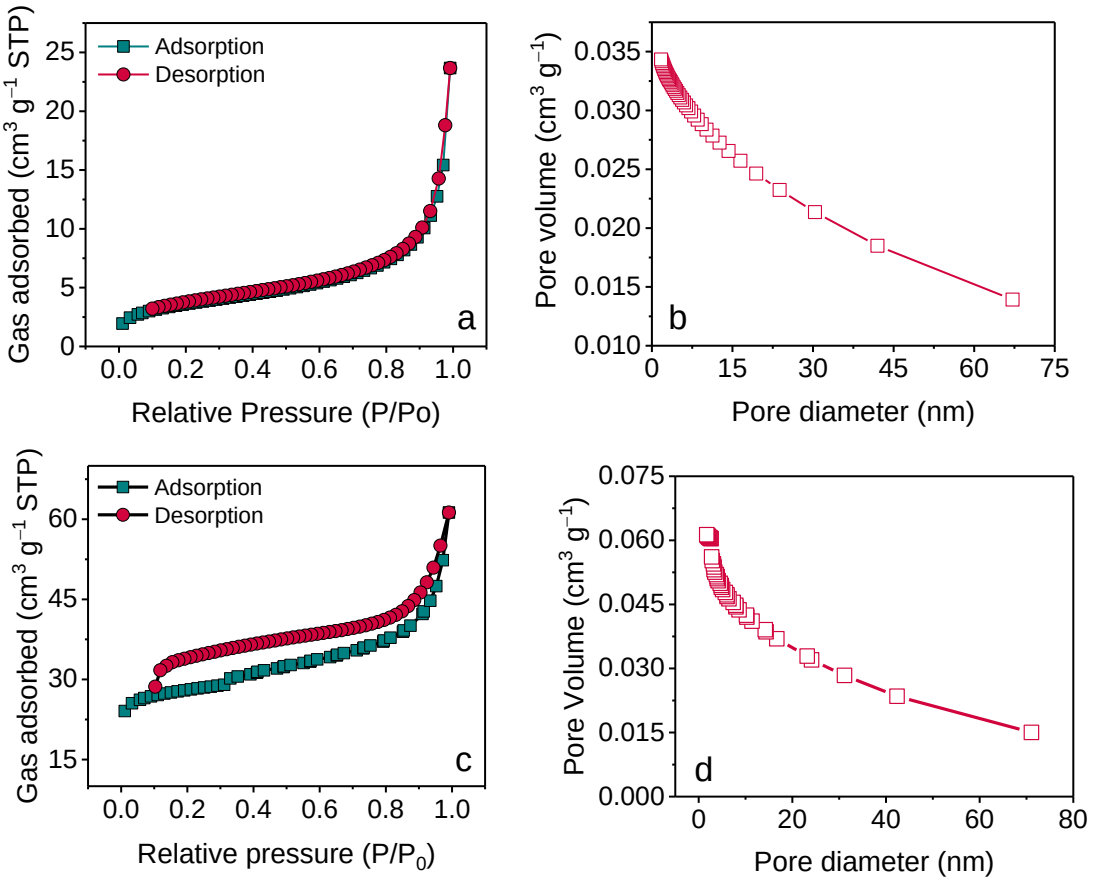

Figure S6. Nitrogen adsorption–desorption isotherms of (a) AMS and (c) NSCS. Pore volume versus pore diameter of (b) AMS and (d) NSCS.

XPS analysis of NCS

The doping of N in AMS-derived carbon spheres was analyzed via XPS. The NCS survey spectra confirmed the presence of C, N, and O (Fig. S7a). The deconvoluted C 1s spectra (Fig. S7b) of NCS revealed the presence of C=C, C-N, C=O, and $\pi \rightarrow \pi^*$ transition. The fitted N 1s spectra of NCS clearly revealed the presence of pyridinic-N at 398.4 eV; pyrrolic-N at 399.8 eV; graphitic N at 401 eV; and oxidized nitrogen functionalities at 403 eV (Fig. S7c).[4-5] The N 1s spectra of NCS was different from the N 1s spectra of AMS, indicative of the doping of the N atom at the pyridinic and graphitic positions of the carbon matrix.

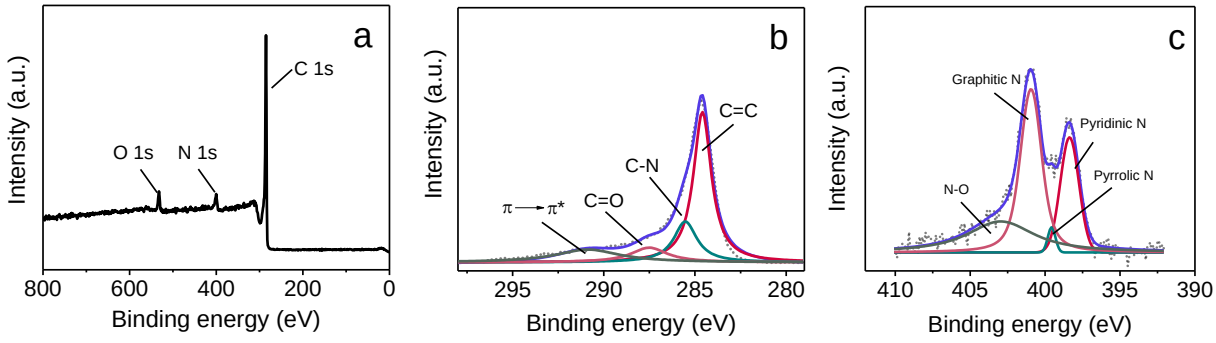

Figure S7. (a) Survey spectra and high-resolution (b) C 1s and (c) N 1s spectra of NCS.

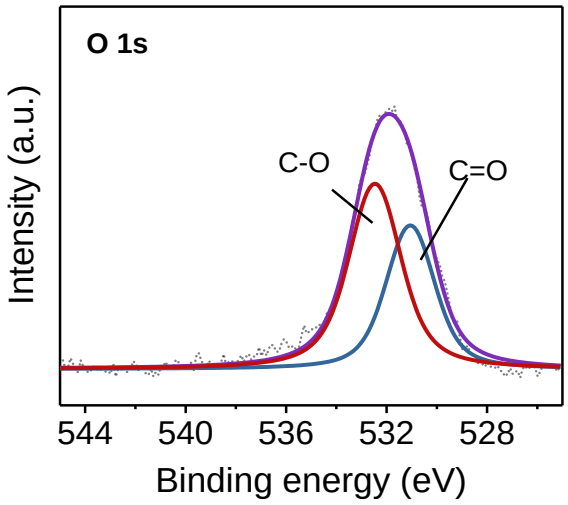

Figure S8. Deconvoluted high resolution XPS spectra of O 1s for NSCS.

Raman spectra of AMS, CPDA, and NSCS

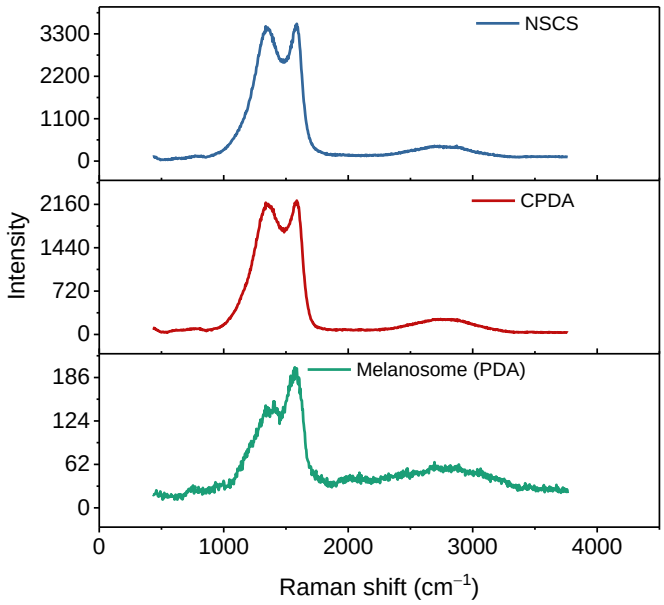

Figure S9. (a) Raman spectra and (b) magnified Raman spectra of melanosomes, C-PDA, and NSCS samples.

Electrocatalytic activity of NCS

In seawater batteries, the air electrode plays a crucial role in ORR and OER reactions associated with the cell discharge and charge. Therefore, prior to cell fabrication, the bifunctional electrocatalytic activity of NCS was examined using the RRDE method in a 0.1 M KOH solution at different rotation speeds using Hg/HgO and Pt as the reference and counter electrodes, respectively. The polarization curves of NCS associated with ORR at different rotating speeds revealed the electrocatalytic activity with an onset potential of −0.176 V versus Hg/HgO, which sharply increased with the potential (Fig. S10a). At −0.9 V versus Hg/HgO, NCS exhibited the maximum current density of −3.2 mA cm^{-2}, which is associated with ORR, at 2500 rpm. Fig. S10b ring current at different rotation speed associated with ORR for NCS as catalyst. The electron-transfer number (*n*) associated with ORR was determined by considering disk and ring

currents of polarization curves at different rotating speeds. The value of *n* was estimated to be 3.3 for NCS catalysts (Fig. S10c). Moreover, the fraction of peroxide ion formation at ring electrode was also estimated using equation (s2) which was found to be ~0.33. Furthermore, OER was also analyzed for NCS to examine its activity in anodic region. The OER polarization curve also revealed the catalytic activity of NCS with an onset potential of 0.37 V vs Hg/HgO in a N_2-purged solution (Fig. S10d). At 0.9 V versus Hg/HgO, NCS exhibited the maximum current density of 0.62 mA cm^{-2}, which is associated with OER. Notably, NCS exhibited decent catalytic activity for ORR but a poor current density for OER.

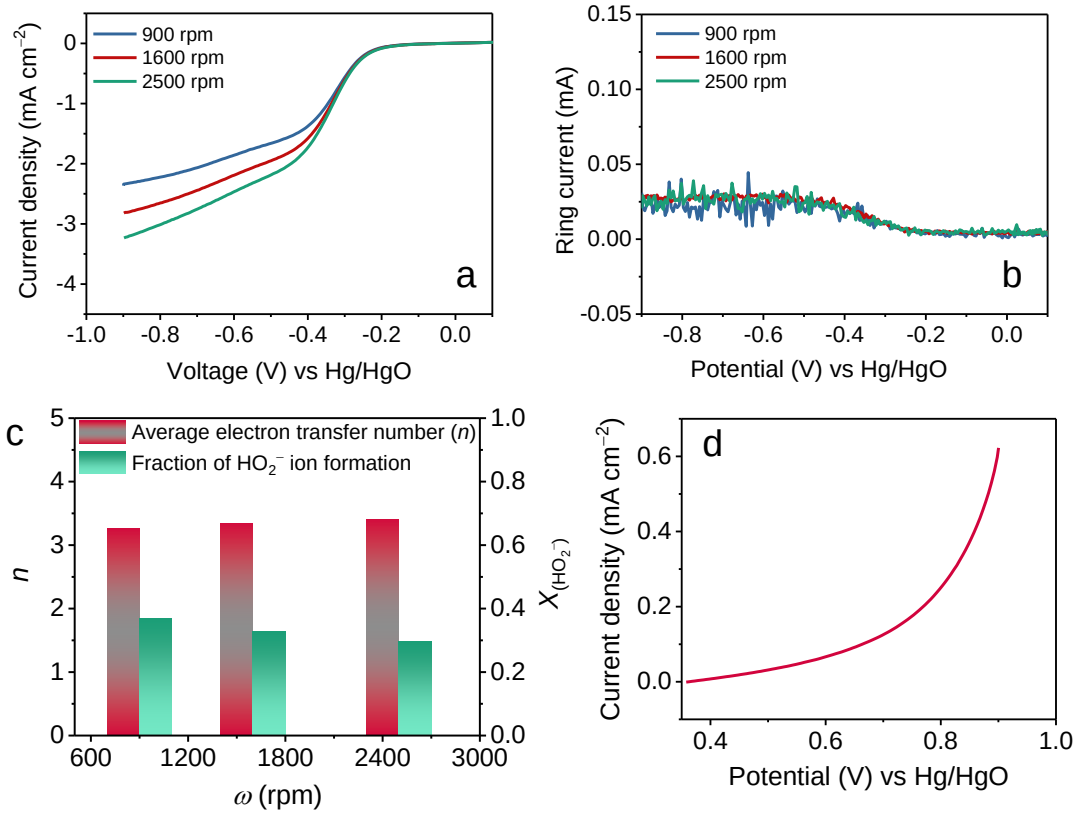

Figure S10. Linear scan voltammograms (LSV) polarization curves for (a) disk and (b) ring currents associated with the ORR of NCS at different rotating speed in 0.1 M KOH at 10 mV s^{-1}; (c) average electron transfer number and fraction of peroxide ion formation for NCS at different rotation rate. (d) OER polarization curves of the NCS electrode at a rotating speed of 1600 rpm with a scan rate of 10 mV s^{-1} in a N_2-saturated 0.1 M KOH solution.

Electrocatalytic activity of NSCS

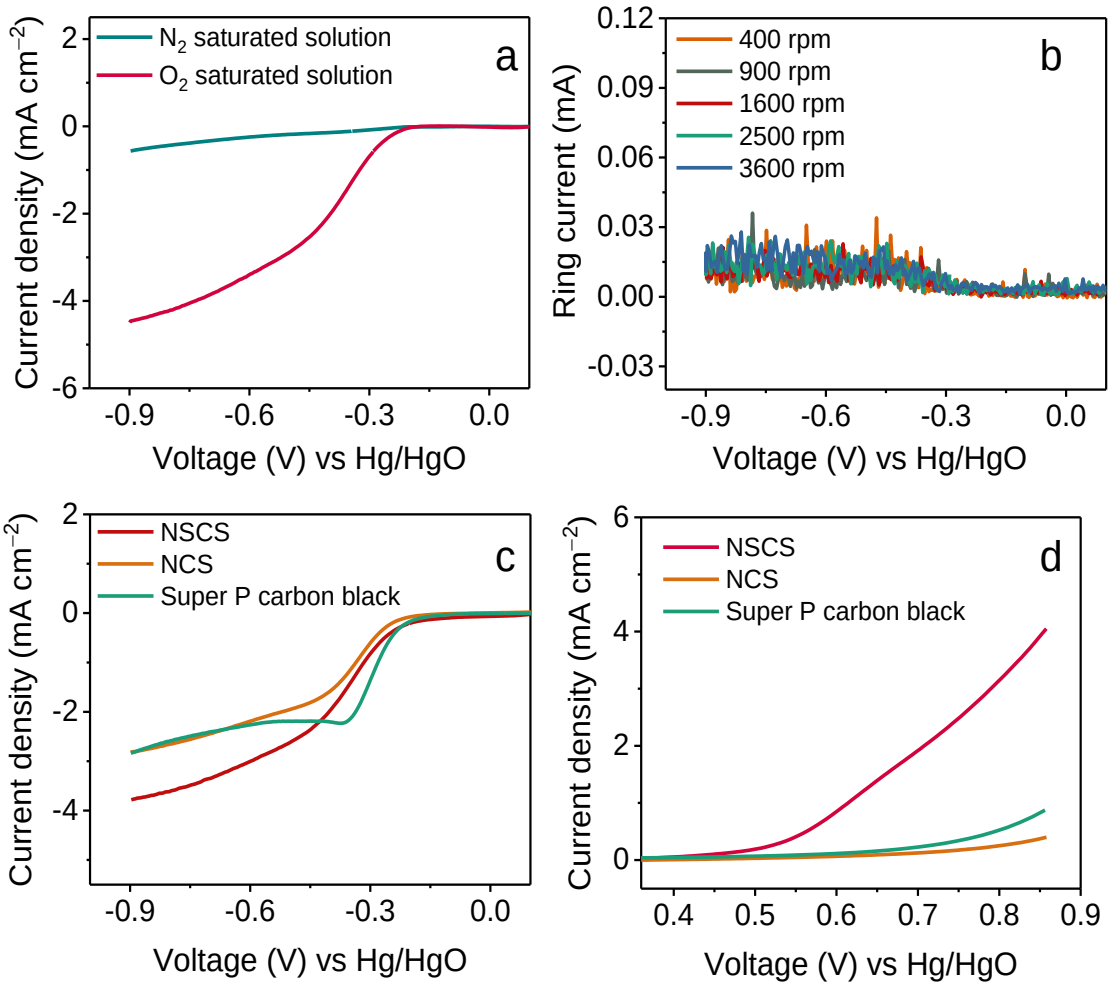

Figure S11. (a) LSV of NSCS in O_2 and N_2 saturated 0.1 M KOH electrolyte at 10 mV s^{-1} scan rate. (b) Ring current associated with ORR for NSCS at different rotation speed. Comparative LSV polarization curves of NSCS, NCS and Super P carbon black associated with (c) ORR and (d) OER at 1600 rpm.

Stability analysis of NSCS for OER

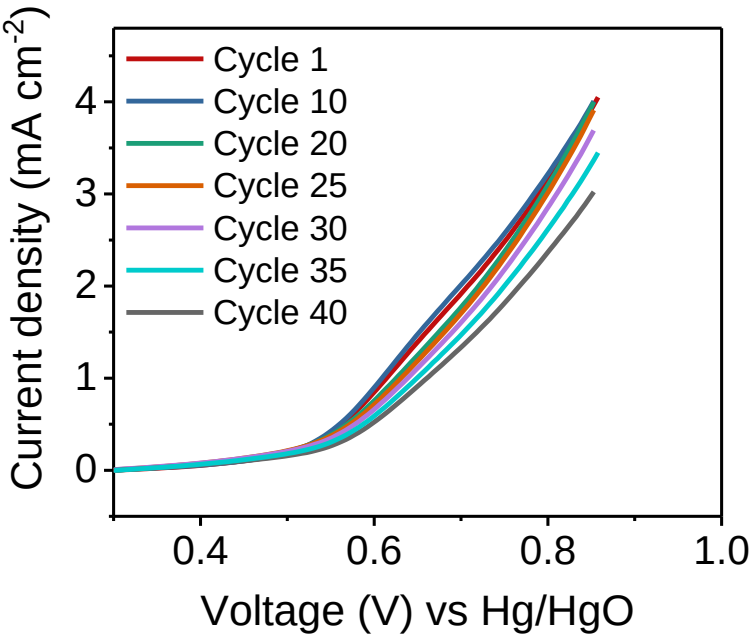

Figure S12. LSV of NSCS associated with OER at different cycles.

Computational modeling and simulation details

Computational modeling

For N,S co-doped graphene, a nitrogen atom was substituted for carbon atoms on a single-layer graphene nanoribbon (GNR) (Fig. S13). Notably, two edge structures were considered (i.e., armchair and zigzag edge). According to the experimental XPS analysis, the nitrogen dopant was in the form of pyridinic N, pyridine-N-oxide, graphitic N, and pyrrolic N.[6] Pyrrolic, pyridinic N, and pyridine-N-oxide were constructed on the edge of GNR, whereas the position of nitrogen was varied for graphitic N. In the case of a sulfur dopant, the structures of thiophene sulfur (S),[7] graphitic sulfur (S),[7-8] and -C-S(O)$_2$-C-[9] were considered. Notably, the remaining carbon atoms

were possible sites for the substitution with sulfur while simultaneously avoiding the possibility for the formation of N-S or S-H bonds (as these bonds were not observed in XPS).

After the structural optimization of N and S co-doped graphene (see "density functional theory (DFT) calculation method" below), the formation energy (E_f) was calculated using the following equation:

$$E_f = E_{tot}^{doped} - E_{tot}^{pristine} + k\mu_C + l\mu_H - m\mu_N - n\mu_S , \qquad \text{(s3)}$$

where E_{tot}^{doped} and $E_{tot}^{pristine}$ represent the total energies of N,S co-doped GNR and pristine GNR, respectively. *k* and *l* represent the number of removed carbons and hydrogens in N,S co-doped GNR for substitution. μ_C and μ_H represent the chemical potentials of carbon and hydrogen, which are defined by the atomic energies of graphite and hydrogen molecules, respectively. *m* and *n* represent the number of nitrogen and sulfur atoms in N,S co-doped GNR, whereas μ_N and μ_S represent the chemical potentials of nitrogen and sulfur, which are defined by the atomic energies of N_2 molecule and α phase of sulfur, respectively. By constructing 608 model systems (all models are not presented here), the results for the formation energy are shown in Fig. S14; the corresponding stable structures are shown in Fig. S15. Sulfur was easily doped in the order of pyridine-N-oxide > pyridinic N > graphitic N in zigzag GNR > graphitic N in armchair GNR > pyrrolic N. Subsequently, the spin density and electrostatic potential for N and S co-doped graphene were estimated for the stable systems (Figs. S16 and S17). Table S1 summarizes the maximum Mulliken spins of above models.

Density functional theory calculation

DFT calculation was performed using the Dmol^3 program.[10-11] The generalized gradient approximation with the Perdew, Burke, and Ernzerhof functional[12] was used to describe

exchange and correlation effects, whereas the electron core was treated by all electrons, including the relativistic effect. The double numerical polarized basis set at the 4.4 level was applied, and the orbital cutoff was set to 4.0 Å . The Brillouin zone was sampled by a Monkhorst–Pack[13] grid with 3 × 1 × 1 and 1 × 3 × 1 *k*-points for armchair and zigzag nanoribbon, respectively, where dipole correction was applied. The vacuum regions of 15 Å and 30 Å , which were parallel and perpendicular to graphene, respectively, were introduced into all systems.

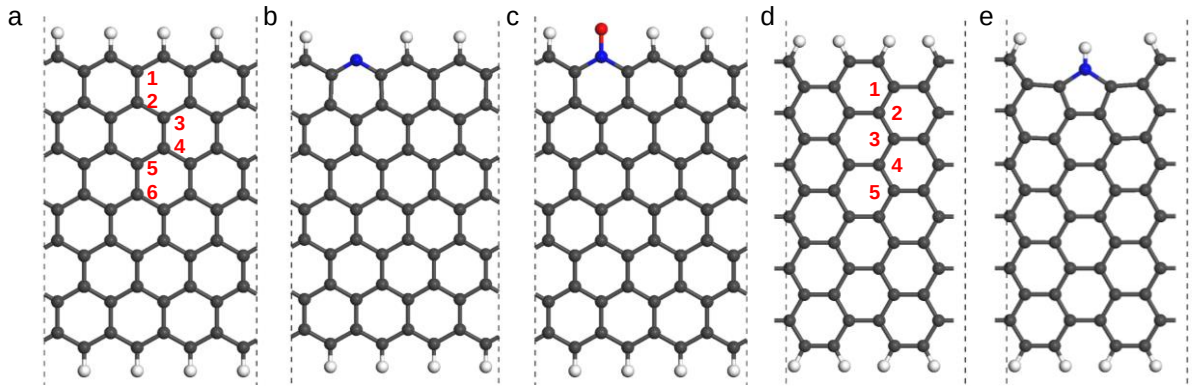

Figure S13. (a) Zigzag graphene nanoribbon, (b) pyridinic N, (c) pyridine-N-oxide, (d) armchair graphene nanoribbon, and (e) pyrrolic N, used in DFT calculations. Red numbers in (a) and (d) represent the substitution sites for graphitic N. Dark gray, white, blue, and red spheres represent carbon, hydrogen, nitrogen, and oxygen atoms, respectively.

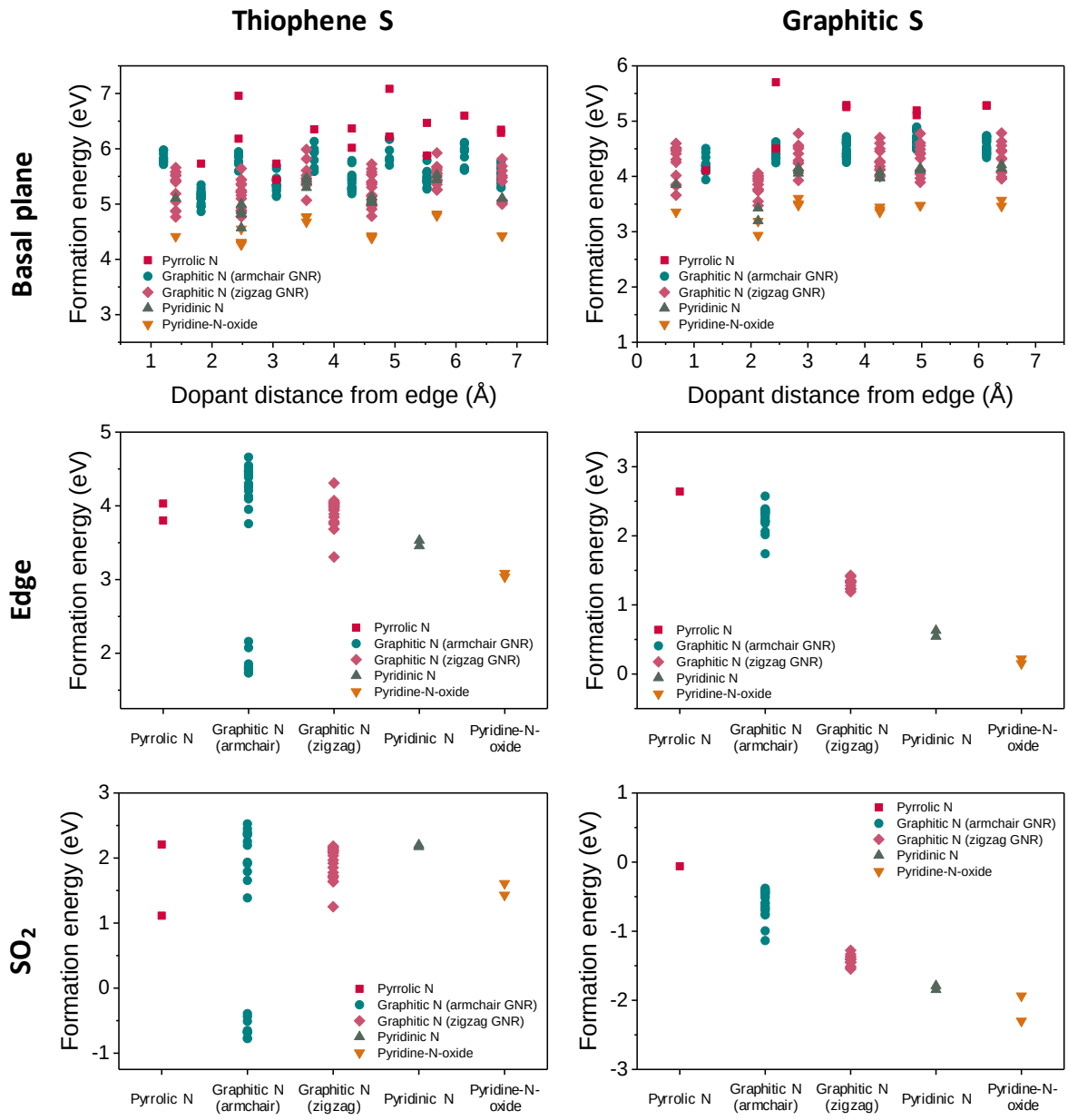

Figure S14. Formation energies of N,S co-doped graphene in terms of the type of functional groups and the position of dopants.

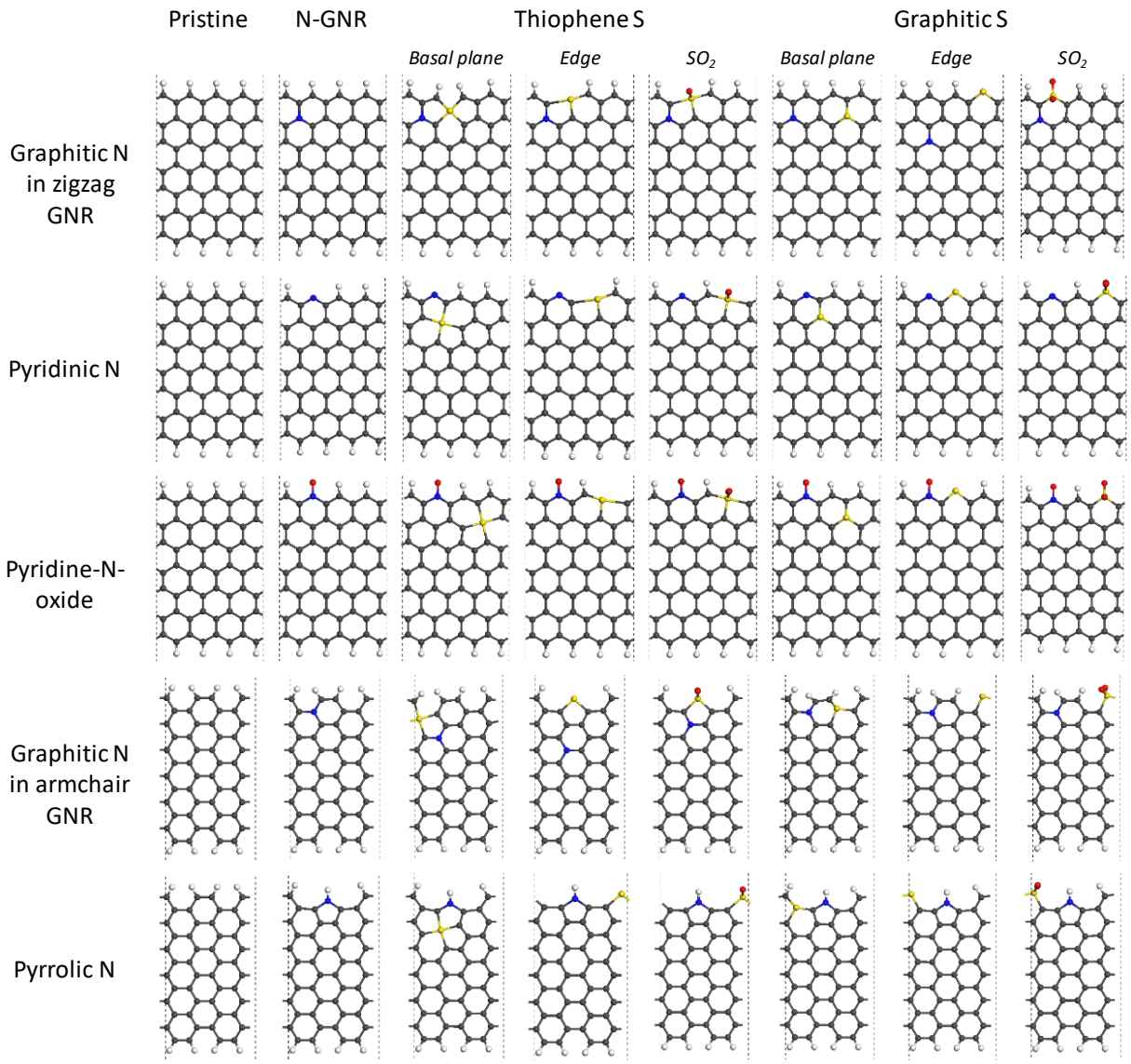

Figure S15. Optimized structures of N,S co-doped graphene, which shows the most stable structure with each functional group identified from Figure S14. Dark gray, white, blue, red, and yellow spheres represent carbon, hydrogen, nitrogen, oxygen, and sulfur atoms, respectively.

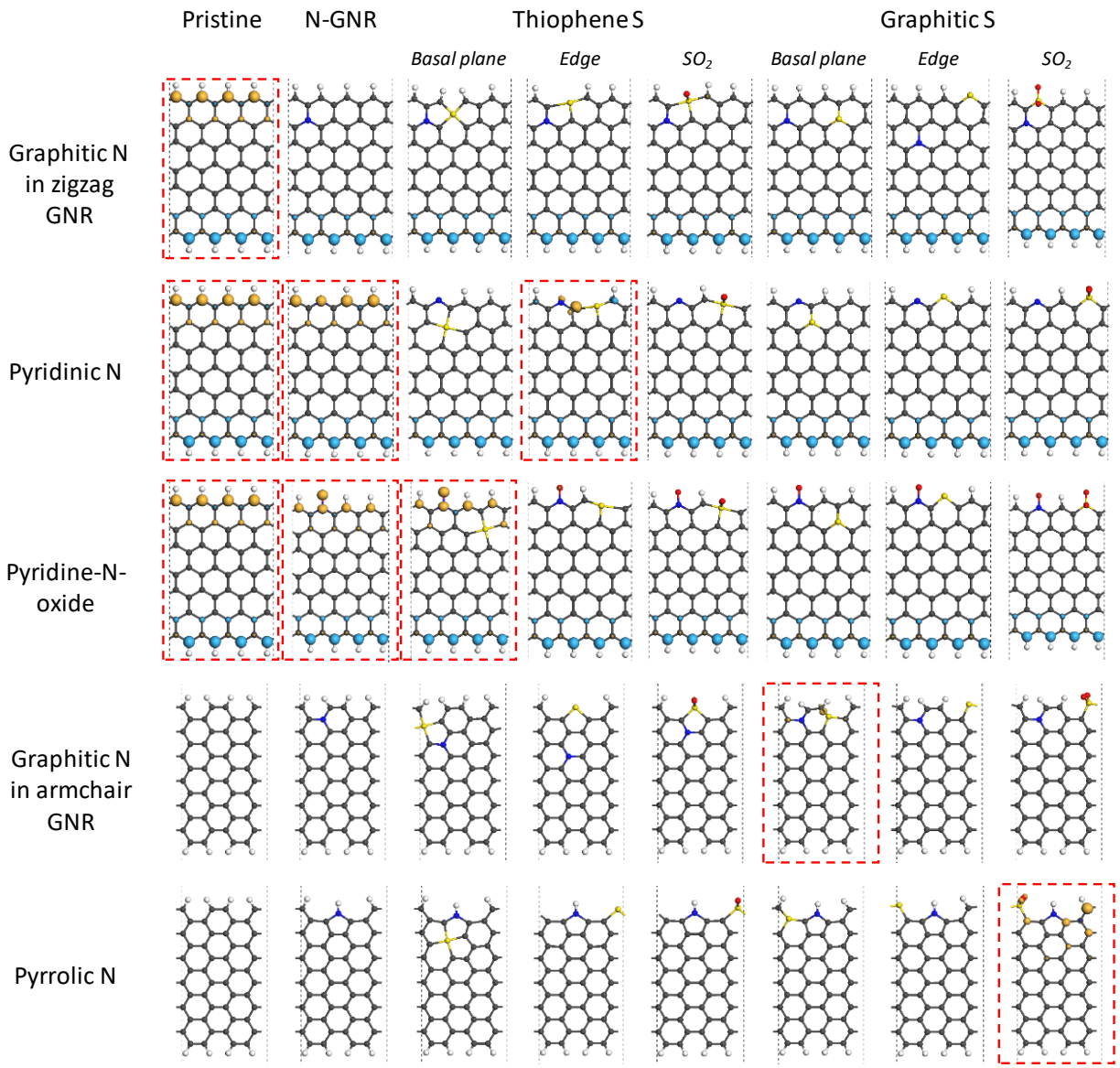

Figure S16. Spin density of N,S co-doped graphene in terms of the type of functional groups. Orange and light blue iso-surfaces represent the spin density with an iso-value of 0.05 *e*/Å ^{3}. Red dashed box represents the models, including high spin density. Dark gray, white, blue, red, and yellow spheres represent carbon, hydrogen, nitrogen, oxygen, and sulfur atoms, respectively.

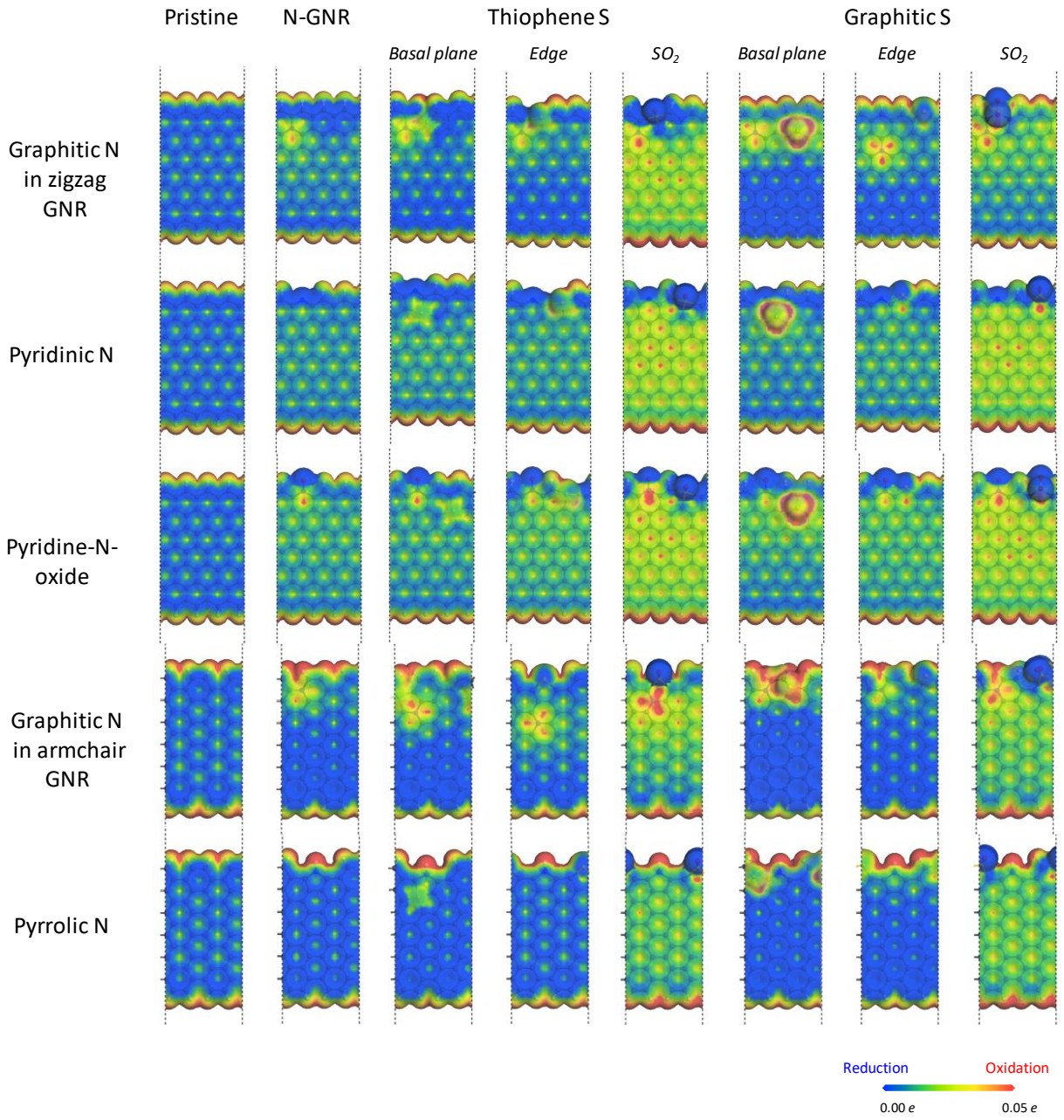

Figure S17. Electrostatic potential maps of N,S co-doped graphene in terms of functional groups. Blue surface represents the zero electrostatic potential, and the red surface represents the region of positive electrostatic potential.

Table S1 Maximum Mulliken spins for zigzag GNR with free S; graphitic N in zigzag GNR with free S; pyridine-N-oxide with free S and thiophene S at the edge; pyridine-N-oxide with free S and thiophene S at the basal plane; armchair GNR with free S; graphitic N in armchair GNR with free S and graphitic S at the basal plane; and pyrrolic N with free S and graphitic SO_2. The term *pristine* represents the model without sulfur.

Model	State of doped sulfur	Max. Mulliken spin
Zigzag GNR	Pristine	0.293
Graphitic N in zigzag GNR	Pristine	0.000
Pyridinic N	Pristine	0.320
	Thiophene S –Edge–	0.221
Pyridine-N-oxide	Pristine	0.223
	Thiophene S –Basal plane–	0.253
Armchair GNR	Pristine	0.000
Graphitic N in armchair GNR	Pristine	0.000
	Graphitic S –Basal plane–	0.094
Pyrrolic N	Pristine	0.000
	Graphitic S –SO_2–	0.325

Seawater-electrolyte-based cell performance analysis using NCS as air electrode

For the seawater battery test, a hybrid cell based on a mixed electrolyte system (seawater as the positive electrolyte, organic electrolyte as the negative electrolyte, and the solid electrolyte membrane as the separator) was constructed, and its performance was analyzed using the galvanostatic charge–discharge method up to 10 h (Fig. S18). The hybrid cell exhibited an overpotential gap of 0.9 V at a current density of 5 mA g^{-1}.

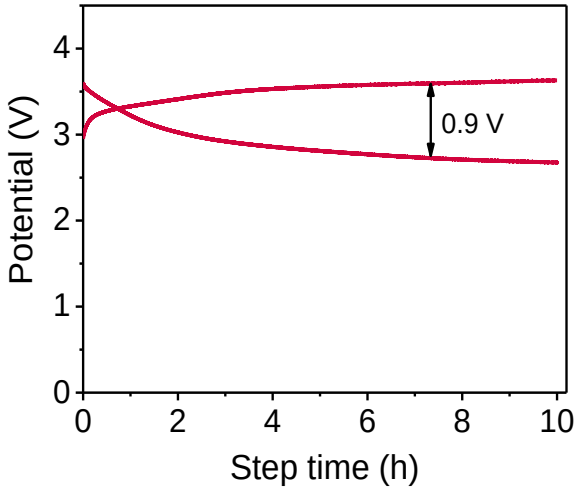

Figure S18. Galvanostatic charge–discharge profile of NCS in the seawater positive electrolyte at a current density of 5 mA g^{-1}.

Rate capability was examined by charging–discharging the half-cell at current densities ranging from 2.5 to 15 mA g^{-1} (Fig. S19a). The seawater positive-electrolyte-based cell exhibited an increase in the overpotential gap from 0.63 to 1.45 V with the increase in the current density from 2.5 to 15 mA g^{-1}. In addition, the cell exhibited the maximum power density of 157 mW g^{-1} at a current density of 120 mA g^{-1} (Fig. S19b). For cell rechargeability, the cyclic stability was investigated by the charge–discharge of the cell up to 50 cycles with charge and

discharge steps of 10 h. The voltage profile did not significantly change up to 50 cycles (Fig. S19c). The overpotential gap and round-trip efficiency for 50 cycles revealed that the overpotential gap of the cell minimally increases from 0.9 to 0.92 V, and the round-trip efficiency (77%) does not change significantly (Fig. S19d). This result revealed the outstanding cycle stability of NCS in the seawater positive-electrolyte-based hybrid cell. The performance observed using NCS as the air electrode and the seawater positive-electrolyte-based cell was extremely good in terms of cycle stability; however, the overpotential gap and round-trip efficiency required further improvement.

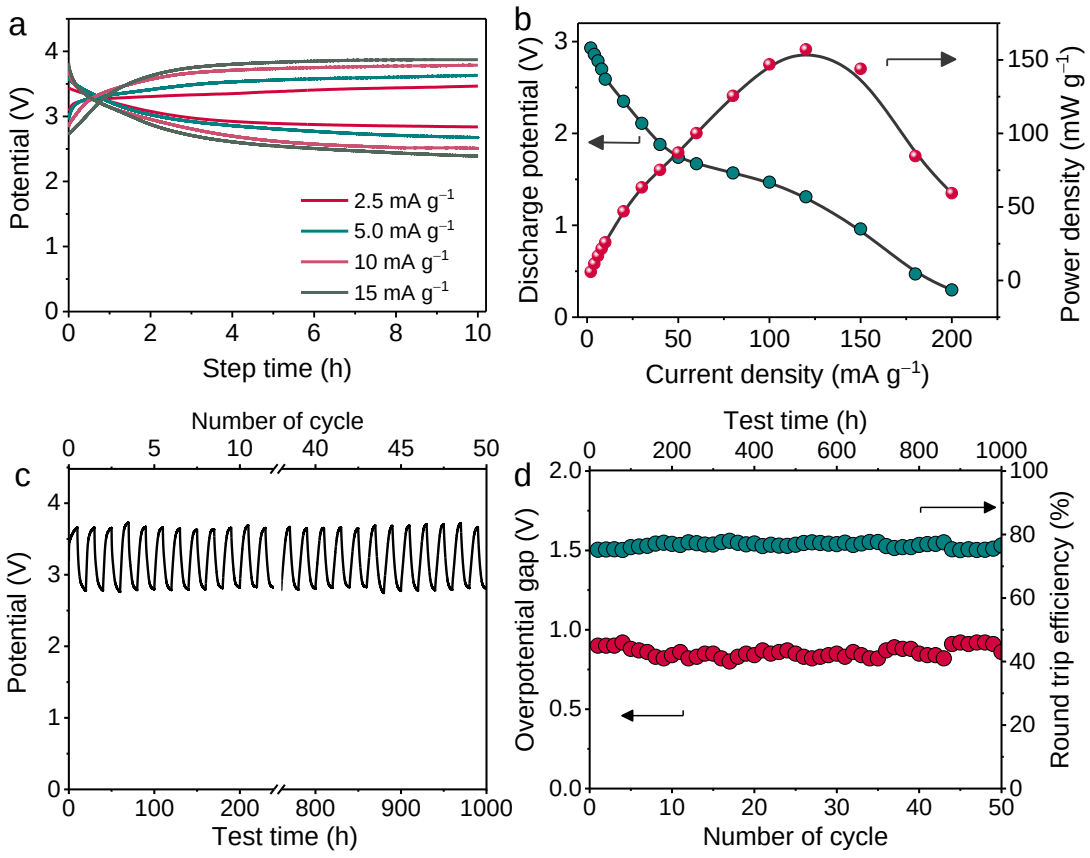

Figure S19. (a) Rate capability test at different current densities, (b) power density plot, (c) voltage profile, and (d) overpotential gap and round-trip efficiency plot for the seawater electrolyte cell using NCS as the air electrode.

Charge–discharge profile of the cell with the NSCS air electrode

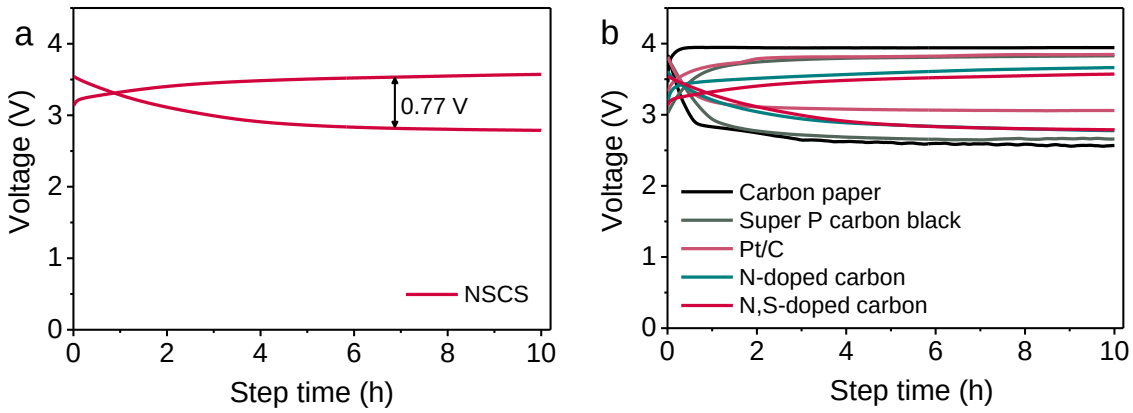

Figure S20. (a) Charge–discharge profile for the first cycle; (b) comparative charge–discharge profile of the cell assembled using bare carbon paper, Super P carbon black, Pt/C, NCS, and NSCS air electrodes at 0.05 mA cm^{-2} with the seawater as the positive electrolyte.

Table S2 Comparison of the previously reported overpotential gaps and cycle stabilities

Air electrode	Current density	Overpotential gap (V)	Voltage efficiency (%)	Cycles	Reference
Carbon paper	0.1 mA cm^{-2}	1.35	67		14
Ag foil	4.76 mA g^{-1}	0.291	90	20	15
Pt/C	0.05 mA cm^{-2}	0.56			16
Carbon felt	0.05 mA cm^{-2}	1.01			16
Hydrophilic carbon[a]	0.025 mA cm^{-2}	1.12	70		17
Porous N-doped carbon	0.01 mA cm^{-2}	0.44		20	18
Oxygen self-doped porous carbon	0.01 mA cm^{-2}	0.47	86		19
NSCS	0.05 mA cm^{-2} or 5 mA g^{-1}	0.56	84	100	This study

[a] Positive electrolyte is 1 M saltwater

Electrochemical impedance spectroscopy analysis

The electrochemical impedance spectroscopy (EIS) technique is a reliable tool to estimate all possible resistance in the cell over a wide range of AC frequencies. EIS spectrum contains different elements which can be related to bulk resistance of material, solution resistance, electrode kinetics, diffusion layer and electrical double layer capacitance. The impedance of cell at any frequency typically contains more than one element thereby making it complicated to analyze the data. Mostly, EIS data was analyzed by equivalent circuit modelling method based on the elements present in the cell. In the current work, the impedance experiments were carried

out at open circuit voltage for seawater electrolyte-based hybrid cell. The fabricated cells have the structure of Na|organic electrolyte|NASICON film|seawater electrolyte|NSCS air cathode. Based on the cell structure and previous literature the equivalent circuit as shown in Fig. S21a was used to analyze different resistances in systems.[20-22] Ivium Technologies Instruments, Iviumstat's software IviFIT equivalent circuit fit module was used to fit the data. We considered bulk resistance (R_E), solution resistance (R_S), resistance related to solid electrolyte interphase (R_I) and charge transfer resistance (R_{CT}) to simulate our data. Moreover, finite-length Warburg element (Z_W) was also considered due to the electrical double layer related diffusion in air cathode.[22]

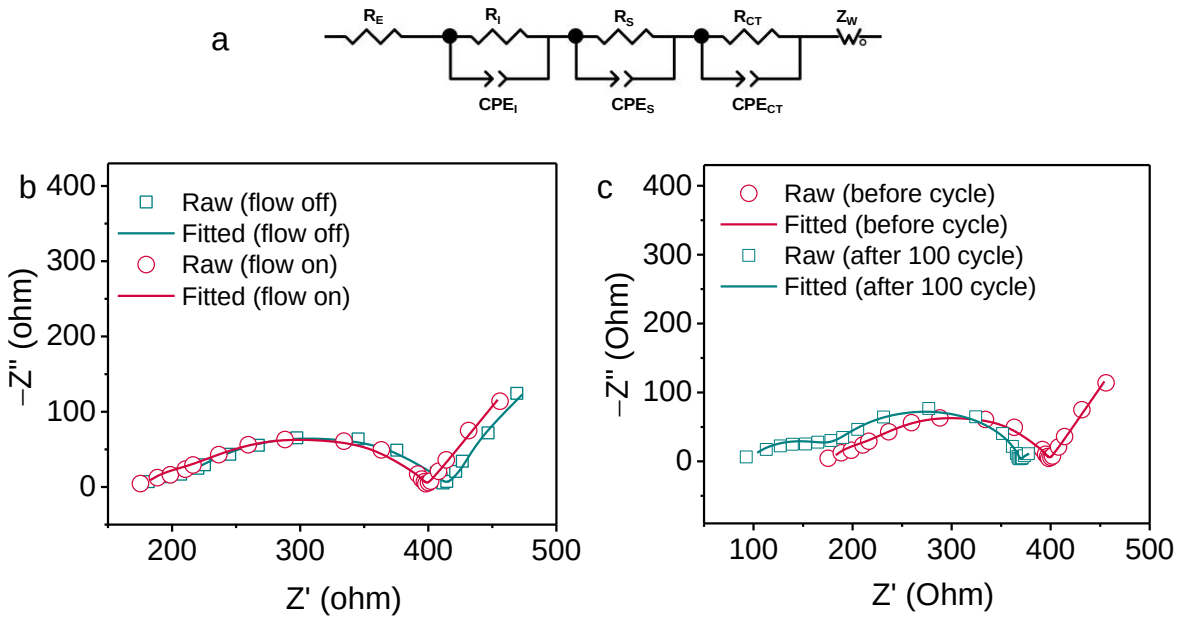

Figure S21. (a) An equivalent circuit that has been utilized to fit the observed data; (b) Nyquist plot of the seawater positive-electrolyte-based cell in the flow-off and -on mode. (c) Nyquist plot before and after cycles of the seawater-electrolyte-based cell in the flow mode. Electrochemical impedance spectra were recorded at the OCV.

Table S3 Estimated values of resistance for the seawater positive-electrolyte-based cell under different conditions (unit is ohm)

Condition	R_E	R_I	R_S	R_{CT}
Flow off	185.7	58.8	110.6	109
Flow on	184.8	56.7	107.8	95.7
After 100 cycles in the flow-on mode	94.9	32.3	89.2	185.8

Post analyses of NSCS electrode and NASICON film

Raman spectra of the electrode before and after cycles

Raman spectroscopy was performed to examine the change in graphitic structure of NSCS after 100 cycles continuous charge-discharge. The obtained Raman spectra for NSCS air electrode before and after cycles is presented in Fig. 22. Neither any significant shift in band nor appearance of any new band was observed in Raman spectra which suggest that the electrode material was electrochemically stable up to 100 cycles.

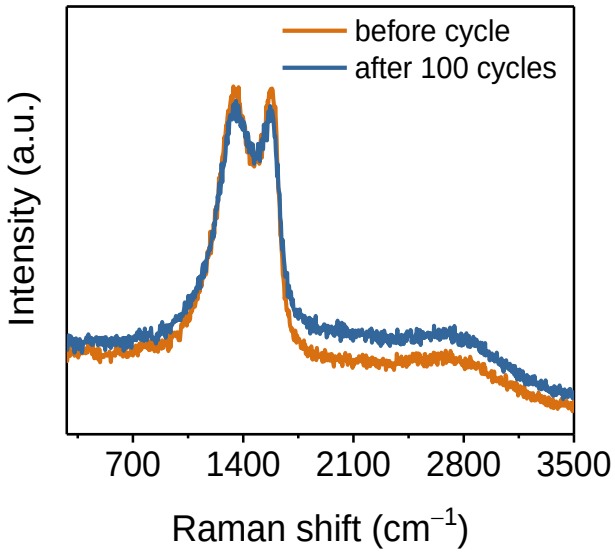

Figure S22. Raman spectra of the NSCS air electrode before and after cycles. The D- and G-bands were observed at the same position even after 100 cycles, revealing the electrochemical stability of NSCS in the seawater electrolyte.

XPS study of NSCS electrode after 100 charge-discharge cycles

Further, XPS was also carried out to investigate the changes in chemical bonding of electrode material. Fig. S23a presents the survey spectra of electrode which suggests presence of C, N, O and S elements. In addition to these elements, few new peaks related to Ca, F and Na appeared in survey spectra which might be due to the use of seawater and organic electrolyte. High resolution deconvoluted C 1s spectra suggests presence of sp^2 hybridized, sp^3 hybridized carbon, C-N, C-S C=O, O-C=O and C-F chemical bonds (Fig. S23b). N 1s spectra can be deconvoluted to three peaks related to pyridinic, pyrrolic and graphitic N (Fig. S23c). In O 1s spectrum (Fig. S23d) displays two peaks related to O-C and O=C chemical bonds. S 2p spectra contains S $2p_{3/2}$, S $2p_{1/2}$ and S-O binding energy peaks (Fig. S23e). However, we also observe Na 1s peak at 1071.7 eV suggest presence of Na^+ species (Fig. S23f).[23]

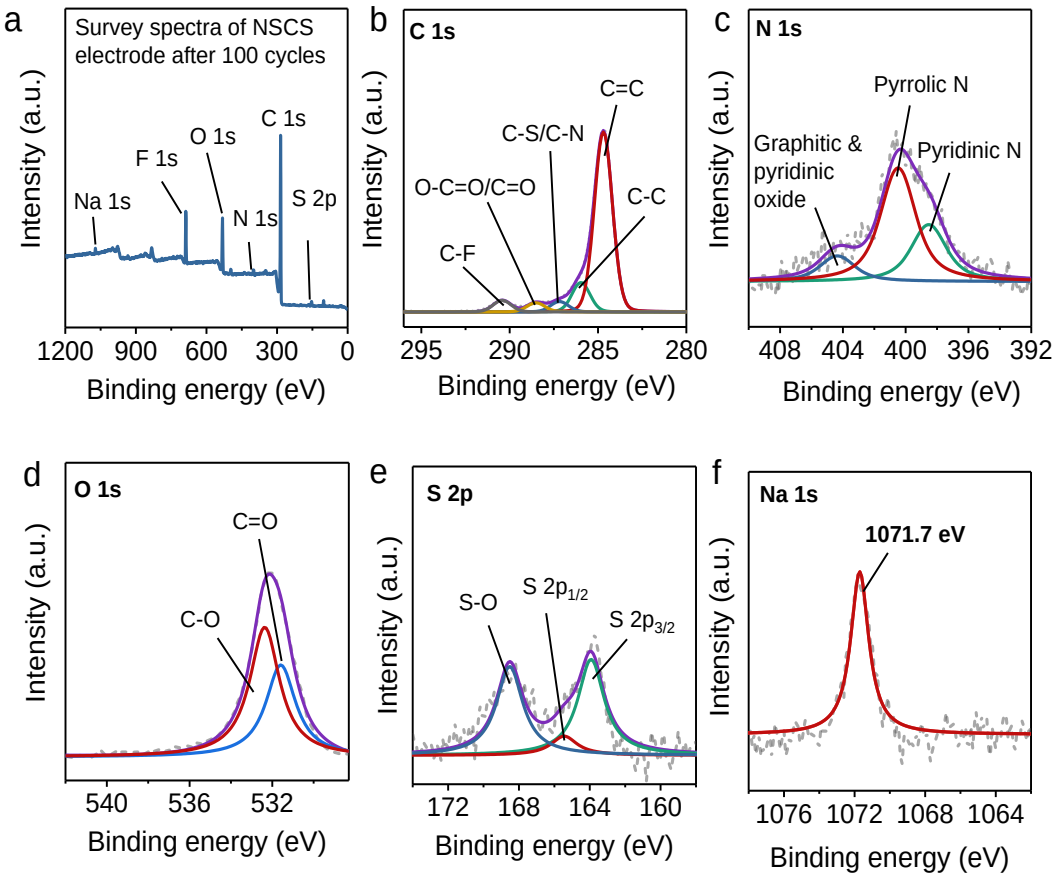

Figure S23. (a) XPS survey spectrum of NSCS air electrode after 100 charge-discharge cycles (1000 h). High-resolution XPS spectra of (b) C 1s, (c) N 1s, (d) O 1s, (e) S 2p and (f) Na 1s for the NSCS electrode after 100 discharge-charge cycles.

Morphology analysis of electrode

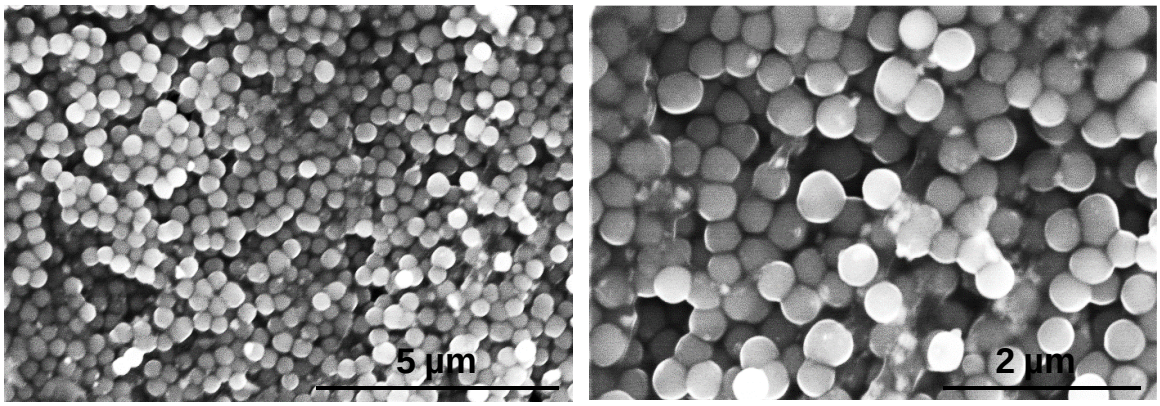

Figure S24. SEM image of the NSCS air electrode after 100 cycles. The morphology did not change significantly.

XRD analyses of NASICON film

NASICON ($Na_3Zr_2Si_2PO_{12}$) was prepared by solid state route which involves mixing of $Na_3PO_4 \cdot 12H_2O$, SiO_2 and ZrO_2 and heating at high temperature.[14] The obtained powder was pressed into pellet followed by its sintering. NASICON film, as a sodium ion conductor, was used to fabricate hybrid cell which separates metallic sodium compartment to aqueous compartment and only allows the passage of Na^+ ion. Thus, its stability is crucial for longer run-ups and practical applications. The stability of NASICON film was analyzed by performing its XRD before and after 100 cycles. The diffraction pattern of NASICON as pristine film well matches with the reference JCPDS 33-1313 which suggest formation of NASICON. However, few impurity peaks were also observed related to ZrO_2 (JCPDS 65-1022) which was used to prepare NASICON film. The used film (after 100 cycle) was also analyzed by XRD to examine any changes in crystal structure. Typically, if there is any change in crystal structure, there will be shift in 2θ.[24] However, in our X-ray diffractogram, no shift in 2θ value was observed thereby suggesting the stability of NASICON film in electrochemical conditions.

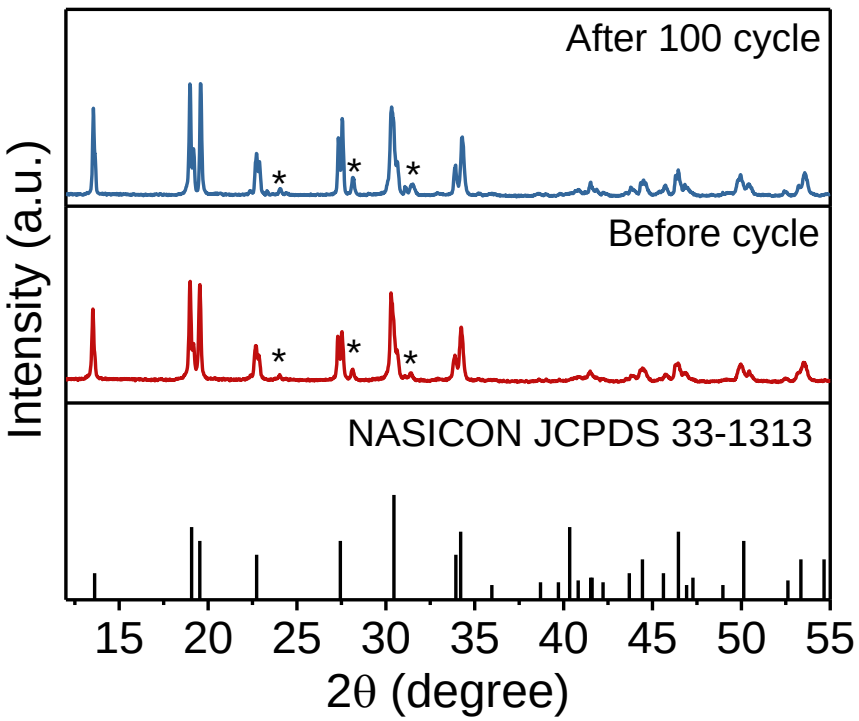

Figure S25. X-ray diffraction of the solid-electrolyte membrane NASICON before and after cycles, revealing the stability of NASICON during electrochemical processes.

References

1. X. Ge, A. Sumboja, D. Wuu, T. An, B. Li, F. W. Th. Goh, T. S. A. Hor, Y. Zong and Z. Liu, *ACS Catal.*, 2015, **5**, 4643−4667.
2. R. Zhou, Y. Zheng, M. Jaroniec and S.-Z. Qiao, *ACS Catal.*, 2016, **6**, 4720−4728.
3. Z. Khan, B. Senthilkumar, S. O. Park, S. Park, J. Yang, J. H. Lee, H.-K. Song, Y. Kim, S. K. Kwak and H. Ko, *J. Mater. Chem. A*, 2017, **5**, 2037-2044.
4. I. Matanovic, K. Artyushkova, M. B. Strand, M. J. Dzara, S. Pylypenko and P. Atanassov, *J. Phys. Chem. C*, 2016, **120**, 29225-29232.
5. P. Chambrion, T. Suzuki, Z.-G. Zhang, T. Kyotani and A. Tomita, *Energy Fuels*, 1997, **11**, 681-685.
6. D. P. Upare, S. Yoon and C. W. Lee, *Korean J. Chem. Eng.*, 2011, **28**, 731-743.

7. D. Higgins, M. A. Hoque, M. H. Seo, R. Wang, F. Hassan, J. Y. Choi, M. Pritzker, A. Yu, J. Zhang and Z. Chen, *Adv. Funct. Mater.*, 2014, **24**, 4325-4336.
8. L. Zhang, J. Niu, M. Li and Z. Xia, *J. Phys. Chem. C*, 2014, **118**, 3545-3553.
9. C. H. Choi, S. H. Park and S. I. Woo, *Green Chem.*, 2011, **13**, 406-412.
10. B. Delley, *J. Chem. Phys.*, 1990, **92**, 508-517.
11. B. Delley, *J. Chem. Phys.*, 2000, **113**, 7756-7764.
12. J. P. Perdew, K. Burke and M. Ernzerhof, *Phys. Rev. Lett.*, 1996, **77**, 3865-3868.
13. H. J. Monkhorst and J. D. Pack, *Phys. Rev. B*, 1976, **13**, 5188-5192.
14. J. K. Kim, E. Lee, H. Kim, C. Johnson, J. Cho and Y. Kim, *ChemElectroChem*, 2015, **2**, 328-332.
15. K. Kim, S. M. Hwang, J.-S. Park, J. Han, J. Kim and Y. Kim, *J. Power Sources*, 2016, **313**, 46-50.
16. S. M. Hwang, J. Kim, Y. Kim and Y. Kim, *J. Mater. Chem. A*, 2016, **4**, 17946-17951.
17. S. Park, B. SenthilKumar, K. Kim, S. M. Hwang and Y. Kim, *J. Mater. Chem. A*, 2016, **4**, 7207-7213.
18. S. Jeoung, S. H. Sahgong, J. H. Kim, S. M. Hwang, Y. Kim and H. R. Moon, *J. Mater. Chem. A*, 2016, **4**, 13468-13475.
19. S. T. Senthilkumar, S. O. Park, J. Kim, S. M. Hwang, S. K. Kwak and Y. Kim, *J. Mater. Chem. A*, 2017, **5**, 14174-14181.
20. F. Liang and K. Hayashi, *J. Electrochem. Soc.*, 2015, **162**, A1215
21. P. He, Y. Wang and H. Zhou, *J. Power Sources*, 2011, **196**, 5611.
22. S. M. Hwang, W. Go, H. Yua and Y. Kim, *J. Mater. Chem. A*, 2017, **5**, 11592.
23. Y. Jin, M.-K. Han and S.-J. Kim, *Appl. Sci.*, 2018, **8**, 12.
24. Y. Yuan, Z. Zhao, J. Zheng, M. Yang, L. Qiu, Z. Li and Z. Zou, *J. Mater. Chem.*, **2010**, 20, 6772–6779.